Mode jumping in the lateral buckling of subsea pipelines

Zhenkui Wang[a,b], G.H.M. van der Heijden[b,*],

[a] State Key Laboratory of Hydraulic Engineering Simulation and Safety, Tianjin University, Tianjin 300072, China

[b] Department of Civil, Environmental and Geomatic Engineering, University College London, London WC1E 6BT, UK

Corresponding author: G.H.M. van der Heijden, g.heijden@ucl.ac.uk

Abstract

Unburied subsea pipelines under high-temperature conditions tend to relieve their axial compressive stress by forming localised lateral buckles. This phenomenon is traditionally studied under the assumption of a specific lateral deflection profile (mode) consisting of a fixed number of lobes. We study lateral thermal buckling as a genuinely localised buckling phenomenon by applying homoclinic ('flat') boundary conditions. By not having to assume a particular buckling mode we are in a position to study transitions between these traditional modes in typical loading sequences. For the lateral resistance we take a realistic nonlinear pipe-soil interaction model for partially embedded pipelines. We find that for soils with appreciable breakout resistance, i.e., nonmonotonicity of the lateral resistance characteristic, sudden jumps between modes may occur. We consider both symmetric and antisymmetric solutions. The latter turn out to require much higher temperature differences between pipe and environment for the jumps to be induced. We carry out a parameter study on the effect of various pipe-soil interaction parameters on this mode jumping. Away from the jumps post-buckling solutions are reasonably well described by the traditional modes whose analytical expressions may be used during preliminary design.

Keywords: Subsea pipeline; Lateral buckling; Mode jumping; Nonlinear pipe-soil interaction; Breakout resistance.

1 Introduction

Long subsea pipelines are becoming increasingly important for the transport of the hydrocarbon products due to the exploitation of hydrocarbon sources into ever deeper water. To prevent solidification of the wax fraction in these products, subsea pipelines are required to operate under high-temperature and high-pressure conditions. This may lead to excessive axial compressive forces and localised lateral buckling is well-known to occur in exposed subsea pipelines with nonlinear lateral soil resistance [1].

Analytical work on localised lateral, as well as upheaval, thermal pipeline buckling in the literature is often based on Hobbs's work [2]. In this work two main assumptions are made. The first one is that the lateral soil resistance is taken to be constant. The second is that the post-buckling pipeline configuration is of a specific shape, or 'mode', i.e., the deflection has a fixed number of lobes. Hobbs distinguishes four different modes.

Extensions of the analytical work to deformation-dependent lateral resistances, while retaining the modal picture, are considered in [3]. Comparisons with finite-element simulations are conducted in [4]. Various Hobbs modes have also been assumed in imperfection studies including cases of intentional imperfections such as sleepers or buoyancy sections introduced as buckle initiation measures [5-10].

It is good to realise though that for these beam-on-foundation problems there are genuine localised solutions of the equilibrium equation in which the pipeline deflection decays to zero exponentially, in an oscillatory fashion. These solutions are obtained by imposing 'flat', or homoclinic, boundary conditions. They have a large number of alternating lobes (infinitely many for a solution on an unbounded domain), but for realistic physical parameters only a few will be important. No assumption needs to be made on the number of significant lobes; they automatically come out as part of the solution. In long pipelines under thermal loading this localised buckling (either upheaval or lateral) is in fact the natural form of buckling because of the (flat) alignment conditions imposed by the longer structure at the ends of the buckle, and with the pipeline free to find its own mobilisation length.

Genuine localised buckling is considered in [11], although the quoted boundary conditions do not maintain localisation as

parameters of the system are varied. In [12] a nonlinear lateral soil resistance model is employed in the form of a quintic polynomial and localised solutions (homoclinic orbits) are explicitly computed. In [13] we perform a parameter continuation and bifurcation study to obtain load-deflection diagrams for localised solutions of partially embedded pipelines subject to a nonlinear pipe-soil interaction.

Here we continue this study of localised lateral buckling using a realistic nonlinear pipe-soil interaction model for partially embedded pipelines. By not having to make assumptions about the number and nature of the lateral lobes we are in a position to investigate transitions, either gradual or sudden, between the Hobbs modes in typical loading sequences. We find that for soils with appreciable breakout resistance sudden jumps between modes may occur. We perform a parameter study on the effect of various pipe-soil interaction parameters on this mode jumping.

2 Problem modelling

2.1 Mathematical formulation

Consider a pipeline laid on the seabed and subjected to a temperature difference T_0 between the fluid flowing inside the pipe and its environment. An axial compressive strain will accumulate due to the axial resistance between pipeline and seabed. Within the range of linear elastic response, the axial compressive force, P_0, corresponding to this axial strain can be written as

$$P_0 = EA\kappa T_0 \tag{1}$$

where E is the elastic modulus, A is the cross-sectional area of the pipeline and κ is the coefficient of linear thermal expansion.

Under increasing temperature difference, the axial compressive force P_0 increases and at some point buckling may be initiated. For a sufficiently long pipeline, this will be localised buckling with exponentially decaying deflection. For a pipe without imperfections we expect this buckling to occur in the centre of the pipeline. We assume this buckling to be lateral, i.e., horizontal, against the resistance of the surrounding soil, rather than vertical, against gravity. For normal coefficients of friction, the lateral mode occurs at a lower axial load than the vertical mode [1]. In the buckling process a small central segment of the pipe will mobilise laterally. Then, as pipe feeds into the buckle, the axial compressive force in the pipe drops, pulling more pipe into the buckle. This feed-in will be halted at two virtual anchor points at compressive force P_0 bounding the mobilised region. Fig. 1 shows the feed-in region within the larger immobilised pipe segment of length l_s along with the localised buckle and the typical compressive force variation. l_s is sometimes called the slip-length.

Based on the profile of axial force shown in Fig. 1, the axial compressive force $\bar{P}(x)$ can be written as

$$\bar{P}(x) = P + f_A x \quad (0 \le x \le l_s) \tag{2}$$

where P is the axial compressive force at the centre of the buckled section after the buckle occurs. The axial soil resistance f_A is

$$f_A = \mu_A W_{pipe} \tag{3}$$

where μ_A is the axial friction coefficient between pipe and seabed and W_{pipe} is the submerged weight per unit length of the pipeline. Axial force balance gives

$$P_0 = P + f_A l_s \tag{4}$$

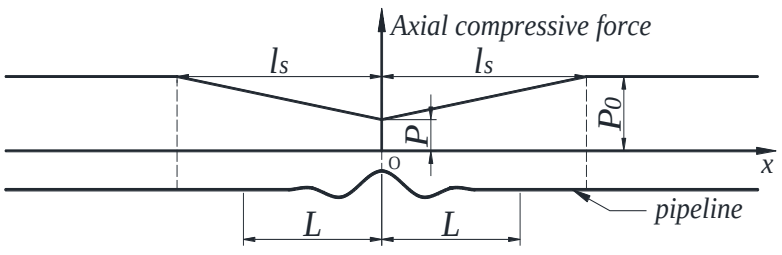

Fig. 1 Axial compressive force distribution of localised lateral buckling.

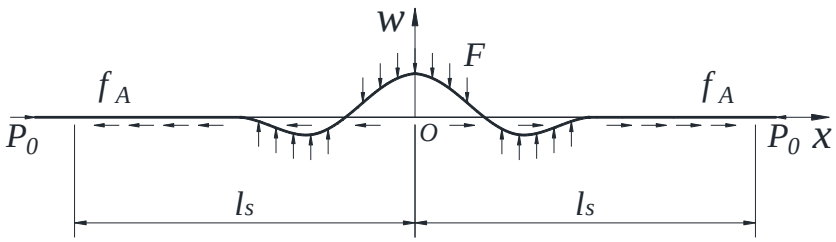

Fig. 2 Configuration and load distribution of localised lateral buckling.

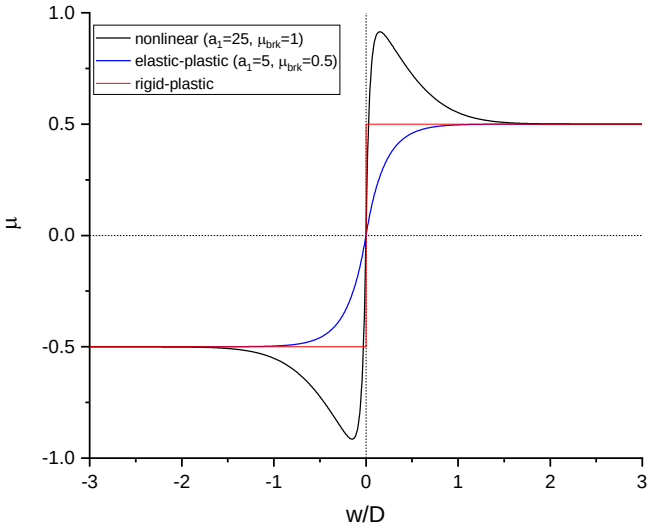

Fig. 3 Different types of pipe-soil interaction models. ($\mu_{res} = 0.5,\ w_{init} = 0.3D.$)

The subsea pipeline subjected to high temperature is idealised as an Euler-Bernoulli beam under axial compression and subjected to a distributed lateral resistance F provided by the soil foundation during the process of localised buckling. Fig. 2 illustrates the typical (symmetric) configuration of lateral buckling for a subsea pipeline resting on the seabed. Thus we have the following equation for the lateral deflection w of the pipeline:

$$EI\frac{d^4w}{dx^4} + \bar{P}\frac{d^2w}{dx^2} + F(w) = 0 \tag{5}$$

where I is the second moment of area of the pipe's cross-section.

For the pipe-soil interaction, the nonlinear model proposed by Chatterjee et al. [14], valid for large deformations, is chosen (see Fig. 3). This model simulates breakout resistance induced by the initial embedment as a result of partial penetration of the pipeline into the soil owing to its self-weight. Once breakout has occurred the lateral resistance drops and approaches a steady residual value. The model can be expressed by

$$\mu = \frac{w}{|w|}\left(\mu_{brk}\left(1 - e^{-a_1\left(\frac{|w|}{D}\right)^{a_2}}\right) + (\mu_{res} - \mu_{brk})\left(1 - e^{-a_3\left(\frac{|w|}{D}\right)^{a_4}}\right)\right) \tag{6}$$

Here μ is the equivalent friction coefficient (taken 0 at $w = 0$), μ_{brk} is the breakout equivalent friction coefficient, μ_{res} is the residual equivalent friction coefficient and D is the external diameter of the pipeline. The quantities $F = \mu W_{pipe}$, $F_{brk} = \mu_{brk}W_{pipe}$ and $F_{res} = \mu_{res}W_{pipe}$ are therefore, respectively, the nonlinear lateral soil resistance, the breakout resistance and the residual resistance for a pipeline laid on an even seabed. F captures both a frictional component of resistance below the pipe and a passive component required to lift and deform the region of soil in front of the pipe [15]. The value of the coefficient a_3, which determines the distance required to mobilise the steady resistance, is in [14] given in terms of the weight of the pipe W_{pipe} and the vertical bearing capacity V_{max} as

$$a_3 = a_5\left(\frac{W_{pipe}}{V_{max}}\right) + a_6 \tag{7}$$

where the values of the two further coefficients a_5 and a_6, for different values of the initial embedment w_{init}, are given by

$$a_5 = 8.2\frac{w_{init}}{D} - 4.9, \qquad a_6 = -5.8\frac{w_{init}}{D} + 4.5 \tag{8}$$

We follow [14] in choosing $a_1 = 25$ and $a_4 = 1.5$, but take $a_2 = 1$ in order to have a finite linear resistance (k in Section 2.2 below), which is physically realistic. We furthermore take $V_{max} = 5W_{pipe}$. We predominantly fix $w_{init} = 0.3D$ and $\mu_{res} = 0.5$ in this study and vary μ_{brk}. Note that when $\mu_{brk} = \mu_{res}$, the nonlinear pipe-soil interaction model degenerates into a monotonic elastic-plastic model (Fig. 3).

We are interested in localised solutions for which the appropriate boundary conditions, to be imposed on Eq. (5), will be specified in Section 2.2. By symmetry of the equation the localised solutions will turn out to be either symmetric or antisymmetric about the midpoint of the buckle. Fig. 2 shows a symmetric configuration; an antisymmetric solution can be seen in Fig. 11(a). In either case, we need only consider half the length of the pipe ($0 \le x \le l_s$). For the geometric shortening u_2 we can therefore write

$$u_2 = \frac{1}{2}\int_0^{l_s}\left(\frac{dw}{dx}\right)^2 dx \tag{9}$$

Compatibility between axial and lateral deformation in the immobilised region $0 \le x \le l_s$ will be employed to derive a relationship between the axial compressive force P at the centre of the pipe and the temperature difference T_0. Compatibility can be expressed as

$$u_1 = u_2 \tag{10}$$

where u_1 is the length of axial thermal expansion within pipeline section region $0 \le x \le l_s$ after buckling occurs. Eq. (10) simply states that the extra length of pipe in the buckle must come from the axial thermal expansion of the mobilised section of pipeline. We have

$$u_1 = \int_0^{l_s}\frac{\Delta\bar{P}(x)}{EA}dx \tag{11}$$

where $\Delta\bar{P}(x) = P_0 - \bar{P}(x)$ is the amount of decrease of axial compressive force along the pipeline after the pipeline buckles. Thus, using Eq. (2), we find

$$u_1 = \frac{f_A l_s^2}{2EA} \tag{12}$$

Combining Eq. (10) and Eq. (12), we obtain

$$l_s = \sqrt{\frac{2EAu_2}{f_A}} \tag{13}$$

which, on using Eq. (1) and Eq. (4), finally gives

$$T_0 = \frac{\left(P + \sqrt{2EAu_2 f_A}\right)}{EA\kappa} \tag{14}$$

The bending moment M along the buckled pipe is calculated as

$$M = EI\frac{d^2w}{dx^2} \tag{15}$$

So the bending stress σ_M along the pipeline can be obtained as

$$\sigma_M = \frac{MD}{2I} \tag{16}$$

The maximum stress σ_m is

$$\sigma_m = \sigma_P + \sigma_{Mm} \tag{17}$$

where the stresses σ_P and σ_{Mm}, resulting, respectively, from the axial force P and the maximum bending moment M_m, are

$$\begin{cases} \sigma_P = \left|\frac{P}{A}\right| \\ \sigma_{Mm} = \left|\frac{M_m D}{2I}\right| \end{cases} \tag{18}$$

2.2 Numerical computation of localised solutions

To compute localised solutions of Eq. (5) we now make the assumption that the axial compressive force is constant in the buckled region and equal to the force at the centre of the buckle, i.e., $\bar{P} = P$. This is standard practice in the pipeline literature [2, 3, 6] and justified by an error analysis in [9, 10]. It is useful to rewrite the fourth-order Eq. (5) as an equivalent four-dimensional system of first-order equations ($w = w_1$):

$$\begin{cases} \frac{dw_1}{dx} = w_2 \\ \frac{dw_2}{dx} = w_3 \\ \frac{dw_3}{dx} = w_4 \\ \frac{dw_4}{dx} = -\frac{1}{EI}(Pw_3 + F(w_1)) \end{cases} \tag{19}$$

Solutions of Eq. (19) are orbits in a four-dimensional phase space with coordinates ($w_1,\ w_2,\ w_3,\ w_4$). The straight pipe solution is represented by the fixed point j = (0, 0, 0, 0). The eigenvalues of the fixed point are:

$$\pm i\sqrt{\frac{P \pm \sqrt{P^2 - 4EIk}}{2EI}} \tag{20}$$

where, since $a_2 = 1$, we have $k = \left(\frac{dF}{dw}\right)_{w=0} = a_1 \mu_{brk} W_{pipe}/D$. We conclude that at the critical load $P = P_{cr}$ with

$$P_{cr} = 2\sqrt{kEI} \tag{21}$$

the eigenvalues λ_i $(i = 1,2,3,4)$ change from a quadruple of complex eigenvalues to two complex conjugate pairs of imaginary eigenvalues (see Fig. 4). This is called a Hamiltonian-Hopf bifurcation [16, 17] and marks the loss of stability of the straight solution. For comparison, the critical load for buckling of a pinned-pinned beam into a pattern of n half sine waves is

$$P_{cr,periodic} = \frac{n^2\pi^2 EI}{L^2} + \frac{kL^2}{n^2\pi^2} \tag{22}$$

It is straightforward to show that $P_{cr} \le P_{cr,periodic}$ for all n.

For later reference we state here that for $P < P_{cr}$ the eigenvalues in Eq. (20) can be written as $\pm\alpha \pm i\omega$, with real α and ω given by

$$\alpha = \frac{\sqrt{2\sqrt{EIk} - P}}{2\sqrt{EI}}, \qquad \omega = \frac{\sqrt{2\sqrt{EIk} + P}}{2\sqrt{EI}} \tag{23}$$

Expansion about the critical load gives

$$\alpha = \frac{\sqrt{P_{cr} - P}}{2\sqrt{EI}}, \qquad \omega = \sqrt[4]{\frac{k}{EI}} - \frac{P_{cr} - P}{4\sqrt{2EIP_{cr}}} + O((P_{cr} - P)^2) \tag{24}$$

confirming the eigenvalue behaviour depicted in Fig. 4.

The symmetry and multiplicity of bifurcating solutions is governed by the symmetry of the system of equations. We have the following two reversing symmetries (i.e., the equations are invariant under the following simultaneous sign changes)

$$R_1\colon\ x \to -x, \quad (w_1,\ w_2,\ w_3,\ w_4) \to (w_1,\ -w_2,\ w_3,\ -w_4) \tag{25}$$

$$R_2\colon\ x \to -x, \quad (w_1,\ w_2,\ w_3,\ w_4) \to (-w_1,\ w_2,\ -w_3,\ w_4) \tag{26}$$

It is well-known that among the solutions bifurcating from the trivial straight solution at $P = P_{cr}$ into the region of the complex quadruple of eigenvalues (here the parameter domain $P < P_{cr}$) are so-called homoclinic orbits that leave the unstable fixed point in the plane spanned by the eigenvectors corresponding to the unstable eigenvalues (with positive real part), make a large excursion in the phase space and then return to the fixed point in the plane spanned by the eigenvectors corresponding to the stable eigenvalues (with negative real part) [17, 18]. These solutions thus approach the straight solution in both limits $x \to \pm\infty$ and are therefore also called localised solutions. Because of the above reversing symmetries, both a symmetric (R_1-reversible) and an anti-symmetric (R_2-reversible) solution bifurcates. Half these localised solutions are shown in Fig. 5(a), while the corresponding half orbits in (a two-dimensional projection of) the phase space are shown in Fig. 5(b). Note that the homoclinic orbits spiral out of (and back into) the fixed point because of the complex eigenvalues.

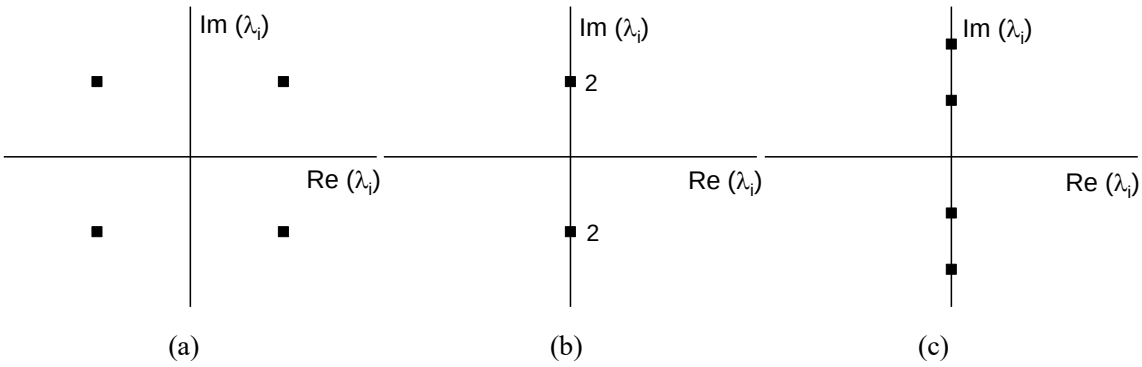

Fig. 4 Behaviour of eigenvalues at the Hamiltonian-Hopf bifurcation. (a) $P < P_{cr}$. (b) $P = P_{cr}$. (c) $P > P_{cr}$.

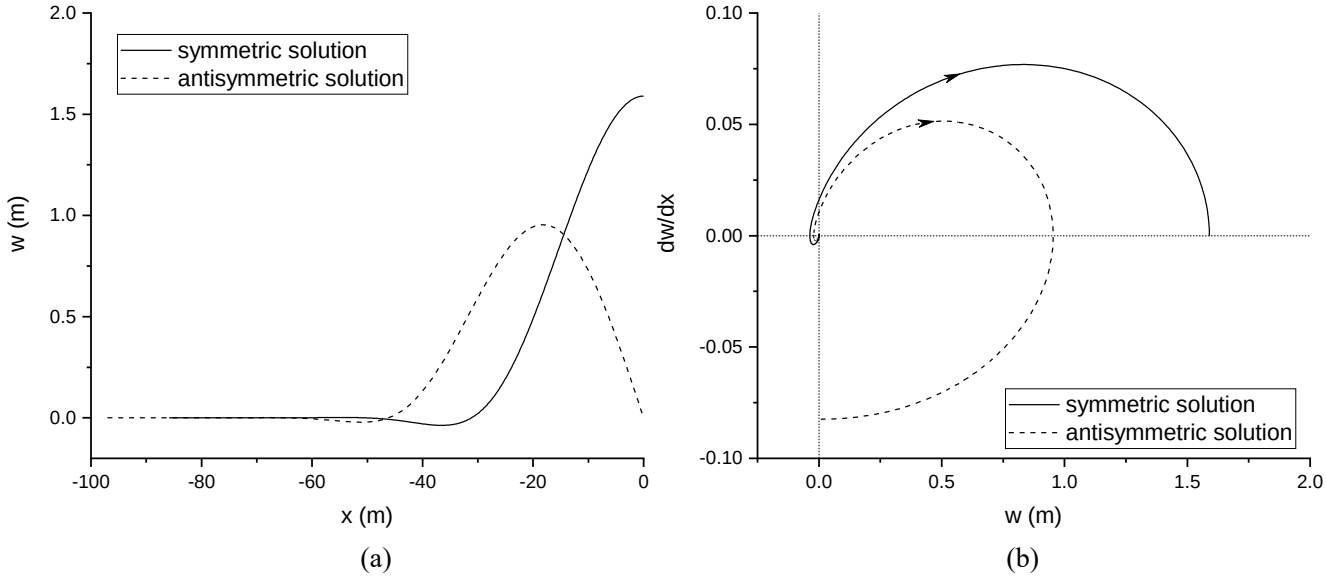

Fig. 5 Typical solution obtained by the shooting method. (a) Deformed shapes. (b) Homoclinic orbits in phase space. ($\mu_{brk} = 2.0,\ \mu_{res} = 0.5,\ w_{init} = 0.3D,\ P = 0.4$ MN.)

For $P < P_{cr}$ we compute approximate (half) homoclinic solutions as in Fig. 5(a) by formulating a shooting method on a truncated x interval $[-L, 0]$. Here L, the half length of the homoclinic solution, is chosen large enough that the solution is well-localised in the sense that it is very nearly decayed to the trivial straight solution j at $x = -L$, but smaller than l_s (see Fig. 1). Thus we specify initial conditions

$$w(-L) = j + \varepsilon(v_1 \cos\delta + v_2 \sin\delta) \tag{27}$$

where $v_1 \pm iv_2$ are eigenvectors corresponding to the eigenvalues $\alpha \pm i\omega$ of j. One might call these homoclinic boundary conditions. ε is a small constant, while δ and L are two shooting parameters that are initially guessed and iteratively updated by means of two further boundary conditions at $x = 0$. The parameter δ is the angle about the fixed point where the outward spiraling homoclinic orbit cuts the circle of radius ε around the fixed point in the unstable eigenspace. For the required two boundary conditions we take advantage of the symmetry properties in Eq. (25) and Eq. (26) to impose

$$\begin{cases} w_2(0) = 0 \\ w_4(0) = 0 \end{cases} \tag{28}$$

for symmetric solutions and

$$\begin{cases} w_1(0) = 0 \\ w_3(0) = 0 \end{cases} \tag{29}$$

for antisymmetric solutions (see Fig. 5).

The half orbits thus computed can readily be turned into full orbits by appropriate reflection according to R_1 or R_2.

Shooting over half the interval is numerically better behaved than shooting back into the neighbourhood of the unstable fixed point. The constant ε sets the scale of L. We choose $\varepsilon = 10^{-5}$, which is found to yield well-localised solutions for the physical parameters we choose. The parameters used in this study are presented in Table 1. For these parameters and the additional choice $\mu_{brk} = 2$ we have $k = 147601.54$ N/m. For the case $P = 0.4$ MN, shown in Fig. 5, the values of δ and L are listed in Table 2. The eigenvalues corresponding to the unstable manifold of the origin are $\alpha \pm i\omega$, where $\alpha = 0.176830$, $\omega = 0.194209$, and we use

$$v_1 = (0.964902, 0.170623, -0.006222, -0.013971)$$
$$v_2 = (0, 0.187393, 0.066273, 0.010511)$$

in Eq. (27). More details of the numerical method can be found in [17, 18].

Table 1 Physical parameters.

Parameter	Value	Unit
External diameter D	323.9	mm
Wall thickness t	12.7	mm
Elastic modulus E	206	GPa
Steel density ρ	7850	kg/m^3
Coefficient of thermal expansion κ	1.1×10^{-5}	/°C
Axial friction coefficient μ_A	0.5	---

Table 2 Shooting parameters. $P = 0.4$ MN.

Reversible under	δ	L (m)
R_1	2.179396	85.853550
R_2	1.657688	97.014261

3 Post-buckling behaviour of symmetric localised solutions – mode jumping

Fig. 6 shows load-displacement curves for symmetric localised solutions computed using the shooting method described in Section 2.2 and taking μ_{brk} = 1.5. The solution curve emerges from the Hamiltonian-Hopf bifurcation which for the present parameters occurs at $T_{cr} = 131.75$ °C. The analytical mode-1 and mode-3 results obtained by Hobbs [2], employing the rigid-plastic soil model in Fig. 3, are included in the diagrams for comparison. The maximum deflection $w_m = w(0)$ is seen to increase with increasing temperature difference T_0 along branch m-b, as expected for an actual pipe, and to decrease with increasing T_0 along branch m-c. We conclude, therefore, that branch m-b is stable and branch m-c is unstable [13]. T_m is the minimum critical temperature difference for the post-buckled pipeline.

We note that the temperature T_m is much lower than T_{cr}. This is usually the case as a result of the relatively large linear foundation stiffness k, but see Fig. 9 ahead for an exception. This type of subcritical bifurcation is known to be sensitive to imperfections. We expect therefore under practical conditions that due to small imperfections or disturbances the pipeline will buckle into a localised solution once T_0 has exceeded T_m and a stable post-buckling solution is available. The rising part of the solution curve, containing state 'b', is thus the relevant part of the diagram and T_m may, for practical purposes, be considered the critical buckling temperature. The varying shape of the buckle is illustrated in Fig. 6(a).

We see in Fig. 6(a) that along the stable buckling branch m-b, w_m increases under increasing T_0 while staying close to, and slightly below, the path of mode 1, until $T_0(m_2)$. At this critical temperature, w_m jumps from state m_2 to state m_3. After this jump, w_m increases under further increase of T_0, now staying close to, but slightly above, the path of mode 3. Fig. 7 illustrates the change in the localised solution in the jump. We see in Fig. 7(a) that in the jump from state m_2 to state m_3 at $T_0(m_2)$ the central large lobe in the positive direction shrinks while the adjacent small lobe grows. The deformed shape

of state m_2 is close to mode 1, while the deformed shape of state m_3 is close to mode 3. We accordingly call this phenomenon mode jumping. Fig. 7(b) shows that the maximum bending stress in both the positive and the negative directions decreases in the jump from state m_2 to state m_3, which causes the maximum stress σ_m also to have a sudden decrease in this jump. In jumping from state m_2 to state m_3 the small lobe shown in Fig. 7(a) breaks through the breakout soil resistance, so this small lobe deflects around the region of residual resistance in the pipe-soil interaction model.

Fig. 6(b) illustrates that, along the stable buckling branch m-b, the maximum deflection in the negative direction, w_{m2} (defined in Fig. 7(a)), initially increases at a small rate under increasing T_0, until $T_0(m_2)$ is reached. Then, after the jump from state m_2 to state m_3, w_{m2} starts to increase at a relative large rate close to the path of mode 3. Fig. 6(c) shows that the jump in the axial compressive force P is small. P is close to (but larger than) the mode-1 value before the jump and close to (and again larger than) the mode-3 value after the jump. The maximum stress σ_m, shown in Fig. 6(d), is similarly larger than the mode-1 maximum stress before the jump and larger than the mode-3 maximum stress after the jump.

Under decreasing temperature difference T_0 the jump will take place from state m_4 to state m_1 at critical temperature $T_0(m_4)$, effectively representing a jump from mode 3 to mode 1 in Hobbs's classification. Since $T_0(m_4)$ is smaller than $T_0(m_2)$ there is a possibility of hysteresis cycles m_1-m_2-m_3-m_4 under increasing and subsequently decreasing temperature (or vice versa). Fig. 6 shows that in the jump from state m_4 to state m_1, w_m, P and σ_m all experience a sudden increase, while w_{m2} has a sudden decrease. The corresponding change in the localised solution is shown in Fig. 8(a). The central large lobe in the positive direction grows while the adjacent small lobe shrinks. The maximum bending stress in both positive and negative directions have a sudden increase in the jump, as shown in Fig. 8(b). In jumping from state m_4 to state m_1 the small lobe shown in Fig. 8(a) shrinks back from the region of residual resistance in the pipe-soil interaction model.

For antisymmetric solutions a similar mode jumping is observed but at much higher temperatures T_0. It is therefore not as important under typical pipeline operating conditions. We therefore do not separately discuss this phenomenon here and instead combine it with the parameter study in Section 4.

In Fig. 9 we also briefly illustrate the effect of the parameter a_1 in the pipe-soil interaction model, Eq. (6), on the post-buckling behaviour, taking $\mu_{brk} = \mu_{res}$ (i.e., we are considering the elastic-plastic interaction model in Fig. 3). This parameter a_1 affects the linear stiffness k and hence the bifurcation temperature T_{cr}, as confirmed in the figure. We also observe, however, that despite this the physically relevant temperature T_m and stable post-buckling solution curve are essentially unaffected by variation in a_1. This can be explained as follows. For the lowest value of a_1 the residual resistance is reached at a midpoint deflection of about 2D (0.648 m), while for larger values it is reached at even smaller deflections (see Fig. 3). At T_m in Fig. 9 the deflection is about 1 m, so even at this lowest temperature at which a post-buckling solution exists much of the buckle already experiences the full residual resistance. Larger a_1 values (and larger T_0) will therefore not cause a significant change in the post-buckling solution. We also note that for this monotonic elastic-plastic interaction model no mode jumping is observed.

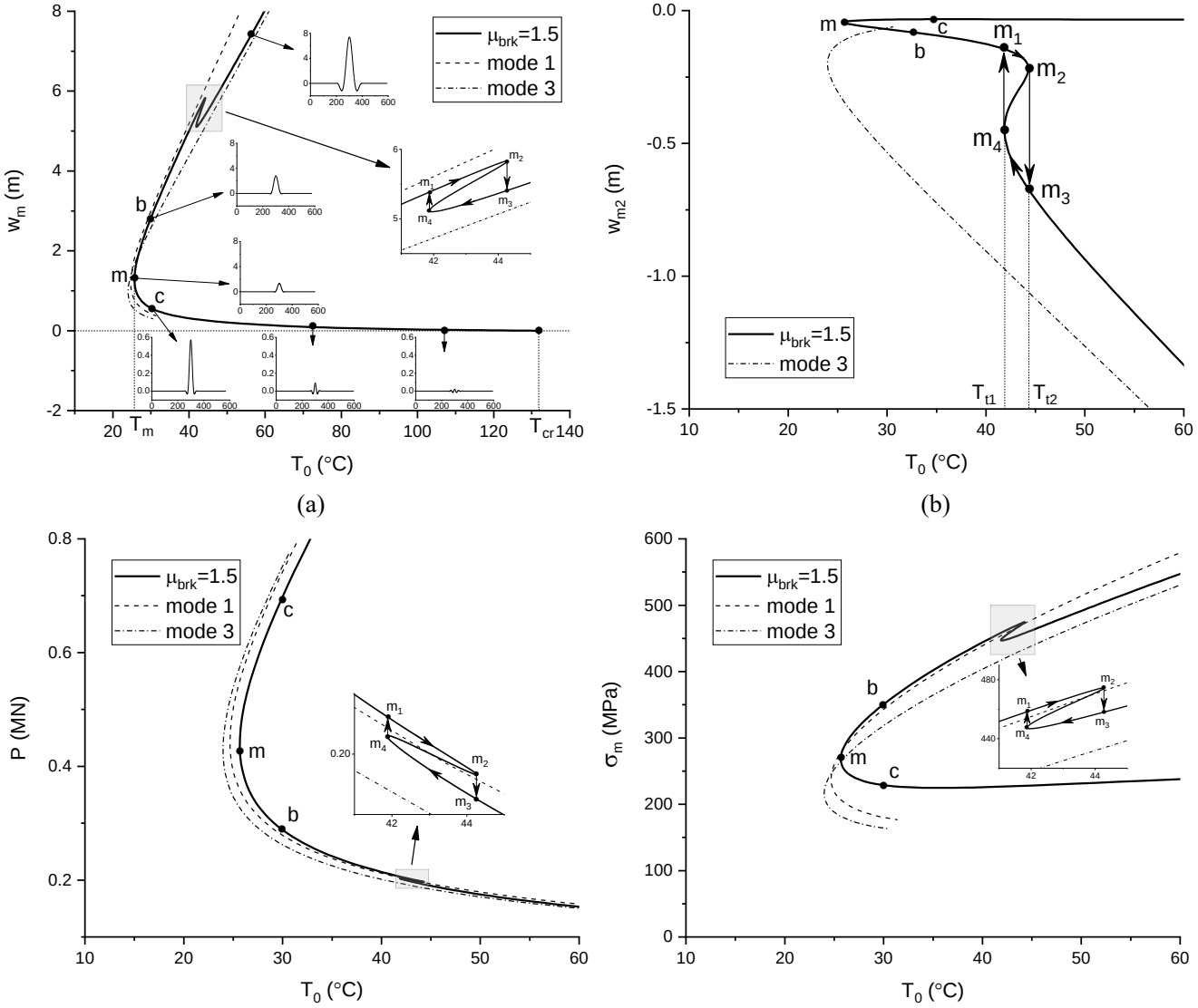

Fig. 6 Mode jumping in the symmetric buckling mode. (a) Maximum deflection w_m. (b) Maximum deflection in the negative direction w_{m2}. (c) Axial compressive force P. (d) Maximum stress σ_m. ($\mu_{res} = 0.5,\ w_{init} = 0.3D$.)

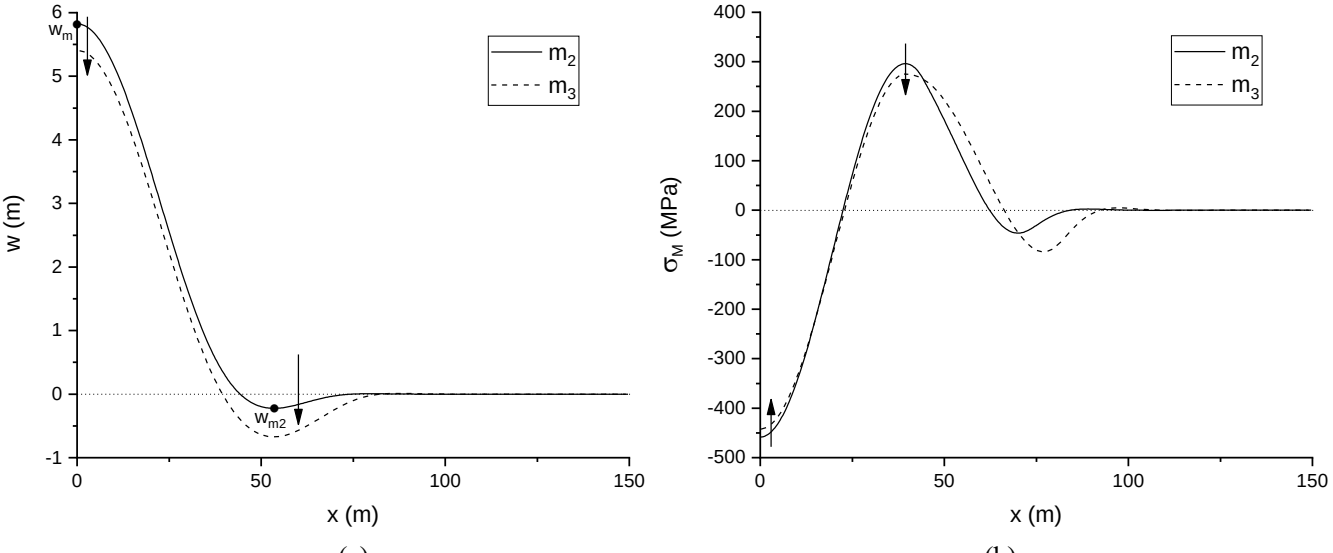

Fig. 7 Localised solutions at labels m_2 and m_3 in Fig. 6. (a) Deformed shapes. (b) Bending stress along the buckled pipeline.

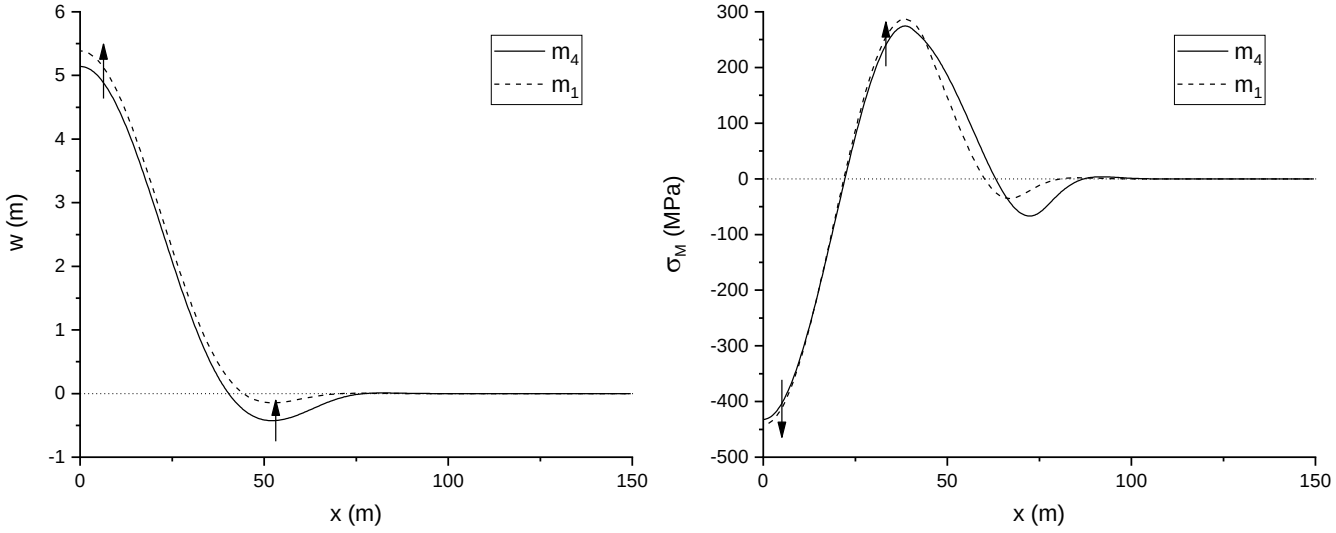

(a) (b)

Fig. 8 Localised solutions at labels m_1 and m_4 in Fig. 6. (a) Deformed shapes. (b) Bending stress along the buckled pipeline.

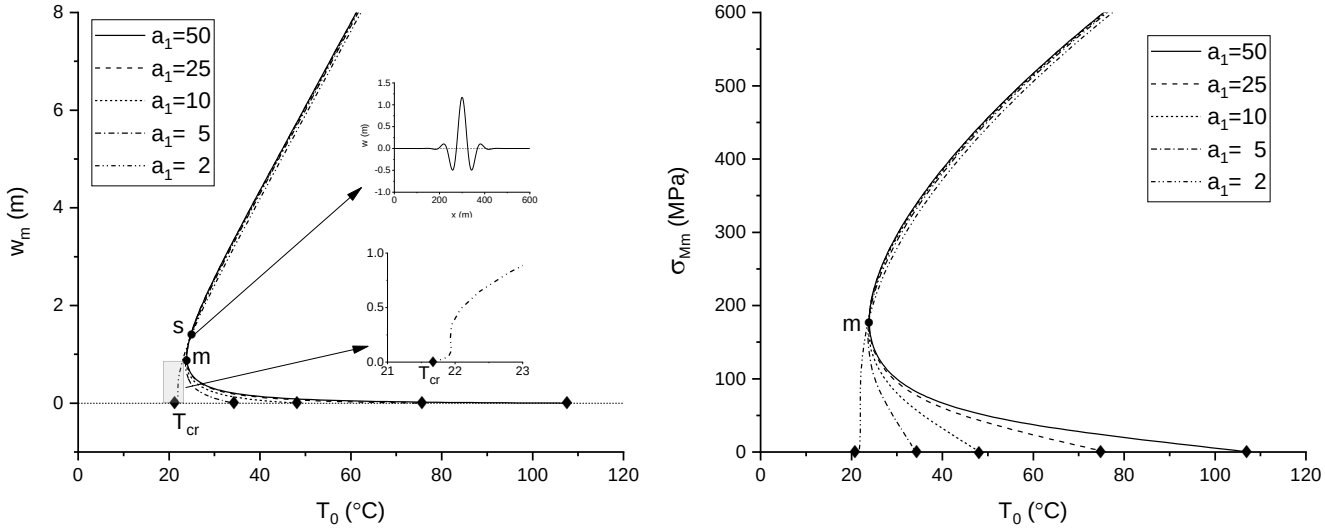

(a) (b)

Fig. 9 Effect of a_1 on the post-buckling behaviour for symmetric solutions. (a) Maximum deflection w_m. (b) Maximum bending stress σ_{Mm}. ($\mu_{brk} = \mu_{res} = 0.5,\ w_{init} = 0.3D$.)

4 Effect of the breakout resistance μ_{brk} on the post-buckling behaviour

For the symmetric buckling mode, the effect of μ_{brk} on the post-buckling behaviour is presented in Fig. 10. Curves for several values of μ_{brk}, are shown in Fig. 10(a) and (b) to illustrate the dependence on μ_{brk} of the temperature T_0 where mode jumping (labelled by $n_i,\ i = 1,\ldots,4$) occurs. For the value $\mu_{brk} = 1.0$ mode jumping occurs at such a low T_0 that modes 1 and 3 are not clearly distinguishable. For all larger values of μ_{brk} a clear mode jumping occurs. The maximum deflection w_m increases with T_0 while staying close to the mode-1 path for $T_0 < T_0(n_i)$ and increases while staying close to the mode-3 path for $T_0 > T_0(n_1)$. We note that larger values of μ_{brk} give larger critical temperatures $T_0(n_i)$. The reason is that it is harder for the lobe to break through the breakout resistance.

We see in Fig. 10(a) that for all μ_{brk} the maximum deflection w_m lies entirely between the paths of modes 3 and 1. The maximum deflections of modes 1 and 3 are therefore useful upper and lower bounds for the case with breakout resistance. Fig. 10(b) reveals that mode jumping appears to occur when the maximum deflection in the negative direction, w_{m2}, is approximately equal to $D/2$, independent of μ_{brk}. The reason is that the nonlinear lateral soil resistance reaches the breakout

resistance at a deflection of about D/2. In the process of mode jumping, the lateral deflection in the negative direction has to overcome this breakout resistance. Fig. 10(c) and (d) display the axial compressive force P and maximum stress σ_m along the solution branch. To present the mode jumping and post-buckling behaviour clearly, detailed curves are only plotted for the single value $\mu_{brk} = 1.5$. Other values give similar results. For comparison, however, curves are included for $\mu_{brk} = 1.0$ and $\mu_{brk} = 3.0$. For $\mu_{brk} = 1.0$, mode jumping occurs for very small T_0, so the post-buckling behaviour is similar to mode 3. For $\mu_{brk} = 3.0$, mode jumping occurs at much higher T_0, so the results shown are before mode jumping and therefore similar to mode 1. We conclude from Fig. 10(c) and (d) that when breakout resistance is taken into account, both the axial compressive force P and the maximum stress σ_m are larger than those of mode 1 before mode jumping, and larger than the values of mode 3 (and lower than those of mode 1) after mode transition. Both P and σ_m are larger for larger breakout resistance, leaving the pipeline in a more dangerous state.

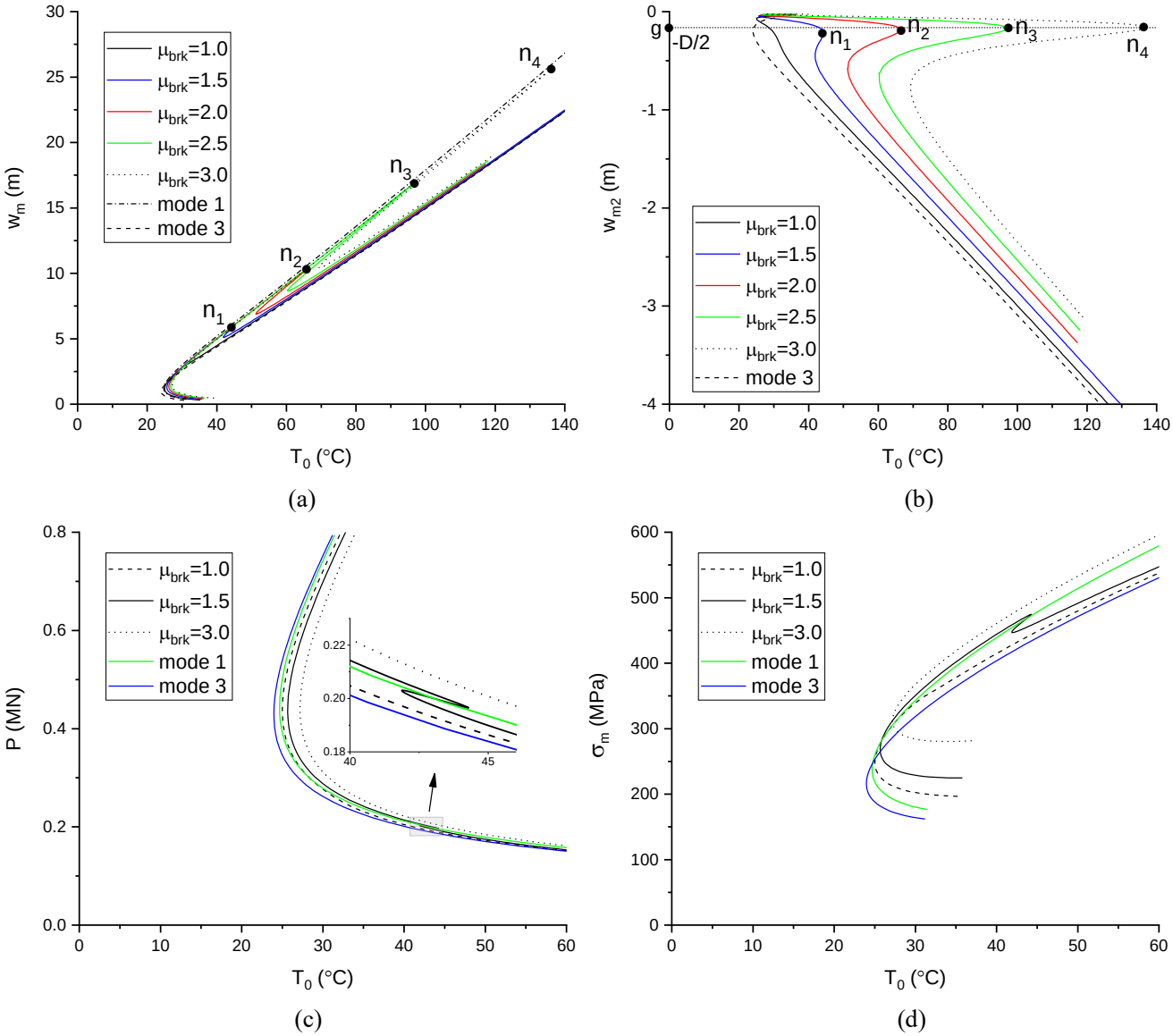

Fig. 10 Effect of μ_{brk} on the post-buckling behaviour for symmetric solutions. (a) Maximum deflection w_m. (b) Maximum deflection in the negative direction w_{m2}. (c) Axial compressive force P. (d) Maximum stress σ_m. ($\mu_{res} = 0.5$, $w_{init} = 0.3D$.)

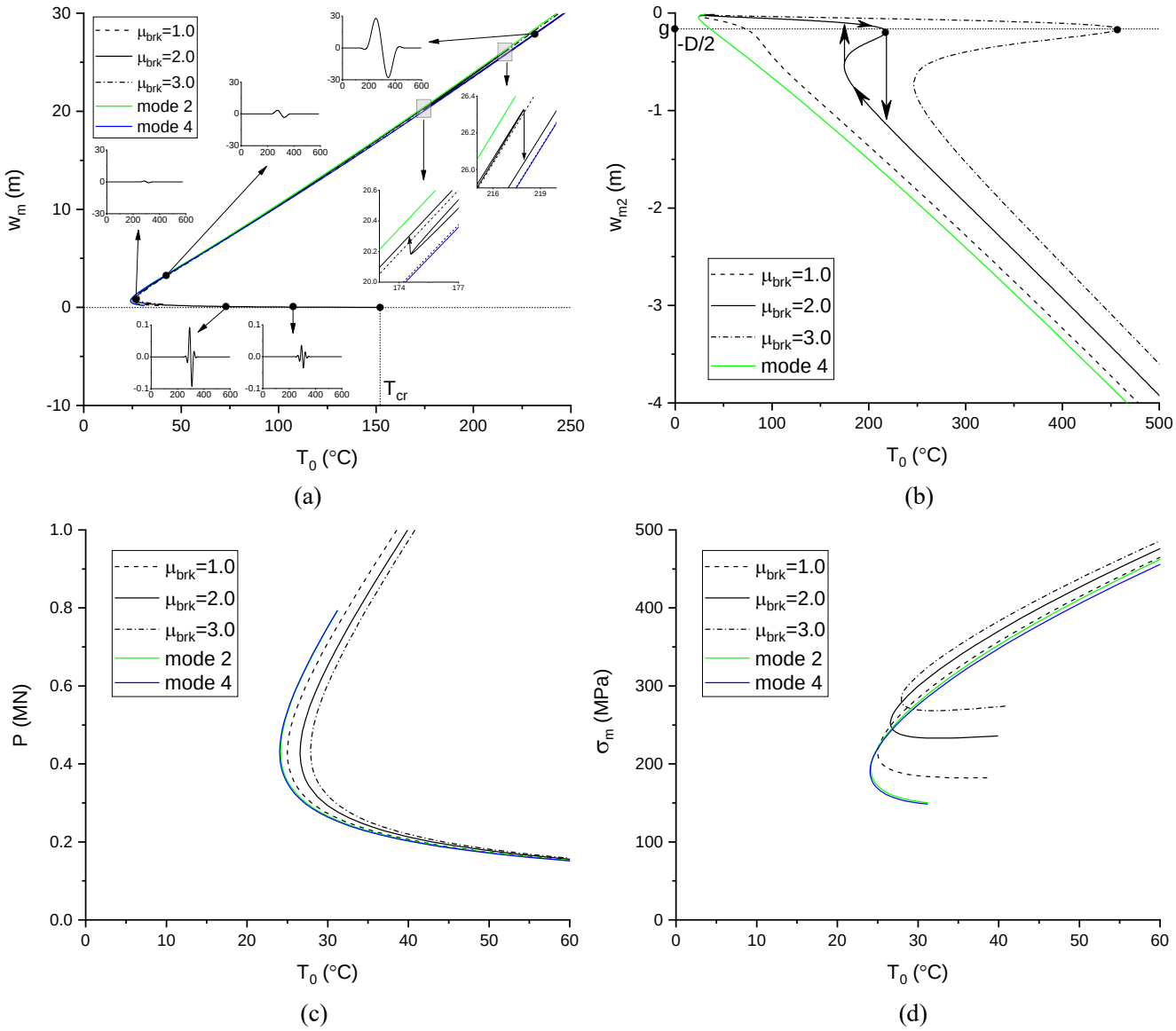

Fig. 11 Effect of μ_{brk} on the post-buckling behaviour for antisymmetric solutions. (a) Maximum deflection w_m. (b) Maximum deflection in the negative direction w_{m2}. (c) Axial compressive force P. (d) Maximum stress σ_m. ($\mu_{res} = 0.5$, $w_{init} = 0.3D$.)

The effect of μ_{brk} on the post-buckling behaviour of antisymmetric localised solutions is presented in Fig. 11. It is seen that mode jumping for these solutions, between approximate modes 2 and 4 in the Hobbs classification, occurs at much higher temperatures T_0 ($T_0 = 174.59\,°C$ and $T_0 = 217.95\,°C$ for $\mu_{brk} = 2.0$). Consequently, for normal operating temperatures, subsea pipelines lie always in the state before mode jumping. It should be pointed out though that for these temperatures the curves for modes 2 and 4 are almost indistinguishable. In Fig. 11(a) we see that, under increasing T_0, the maximum deflection w_m increases while staying close to, and slightly below, the mode-2 path, which gives an upper bound for the cases with breakout resistance. Fig. 11(b) shows that mode jumping again appears to occur when the maximum deflection in the negative direction, w_{m2}, reaches a value of $D/2$, as was also found to be the case for symmetric solutions (see Fig. 10(b)). According to Fig. 11(c) and (d) both the axial compressive force P and the maximum stress σ_m are (slightly) larger than the respective values of the mode-2 paths, and the more so as μ_{brk} increases.

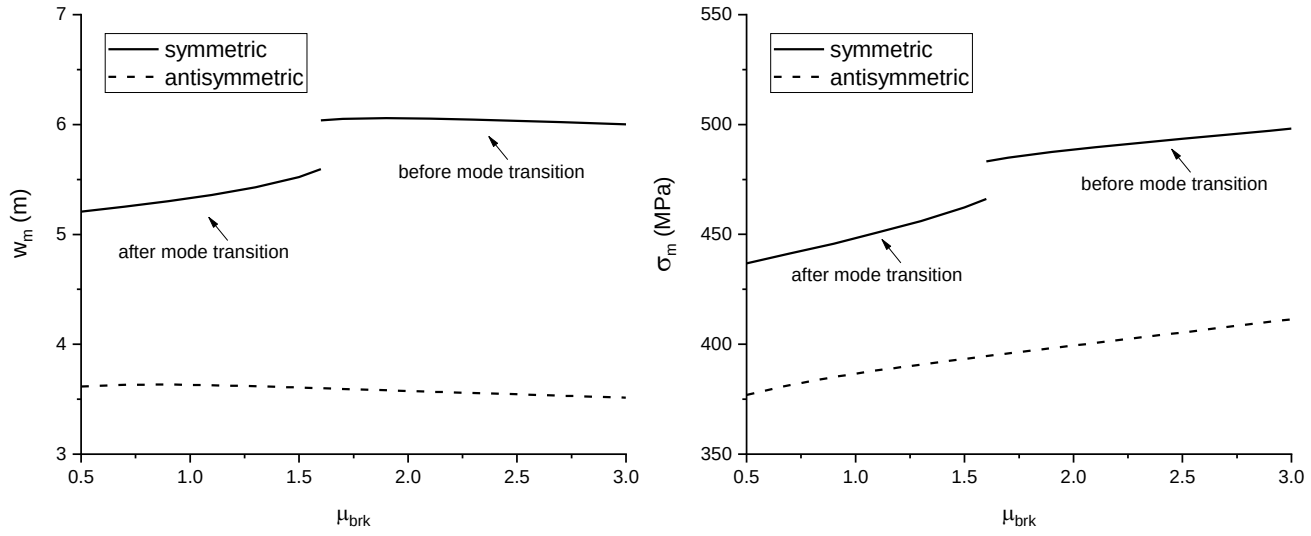

(a) (b)

Fig. 12 Effect of μ_{brk} for symmetric and nonsymmetric solutions. (a) w_m. (b) σ_m. ($\mu_{res} = 0.5,\ w_{init} = 0.3D,\ T_0 = 45$ ℃.)

The effect of μ_{brk} on the maximum deflection w_m and the maximum stress σ_m, at the moderate temperature difference $T_0 = 45$ ℃, is compared for symmetric and antisymmetric solutions in Fig. 12. Note that the plots for the symmetric buckling mode are discontinuous because the parts for large μ_{brk} are obtained before mode jumping, while the parts for small μ_{brk} are obtained after mode jumping. By contrast, for the antisymmetric buckling mode the entire plots are before mode jumping at this temperature. We see in Fig. 12(a) that w_m is much larger for the symmetric solution than for the antisymmetric solution. Correspondingly, Fig. 12(b) shows that the maximum stress σ_m is much larger for the symmetric solution than for the antisymmetric solution, and goes up with μ_{brk}.

A normalised parametric analysis of the effect of μ_{brk} on w_m and σ_m for the symmetric buckling mode is given in Fig. 13. The values of w_m and σ_m are normalised against the corresponding values of modes 1 and 3. The figure shows to what extent the analytical results of modes 1 and 3, obtained with constant lateral resistance, can be used to get a rough estimate for the cases with nonlinear pipe-soil interaction. We see that before mode jumping, at relatively large μ_{brk}, the analytical results of mode 1 can be used to estimate the values of w_m and σ_m with errors less than 5 %. After mode jumping, at relatively small μ_{brk}, the analytical results of mode 3 can be used to estimate the values of w_m and σ_m with errors less than 7 %. The challenge is, of course, to know whether mode jumping has occurred or not. If, after mode jumping, at small μ_{brk}, we use the analytical results of mode 1 to estimate the values of w_m and σ_m, then the errors are less than 20 % and less than 10 %, respectively, getting smaller for larger μ_{brk}. The good news is that the analytical results of mode 1 overestimate the real values, so we obtain a suitably conservative estimate.

The effect of μ_{brk} on the normalised w_m and the normalised σ_m for the antisymmetric buckling mode is shown in Fig. 14. The values of w_m and σ_m are now normalised against the corresponding values of modes 2 and 4. From Fig. 14(a) it follows that when w_m is estimated by the analytical results of modes 2 and 4 the errors are less than 5 %, getting larger for larger μ_{brk}. From Fig. 14(b) it follows that when σ_m is estimated by the analytical results of modes 2 and 4, the errors are less than 7.5 % and less than 9 %, respectively, again getting larger for larger μ_{brk}.

We conclude that the results of pipeline lateral buckling with a nonlinear pipe-soil interaction that takes account of breakout resistance can be roughly estimated by the analytical results of Hobbs's modes 1, 2, 3 and 4 obtained with constant lateral resistance (i.e., with the rigid-plastic pipe-soil interaction model shown in Fig. 3).

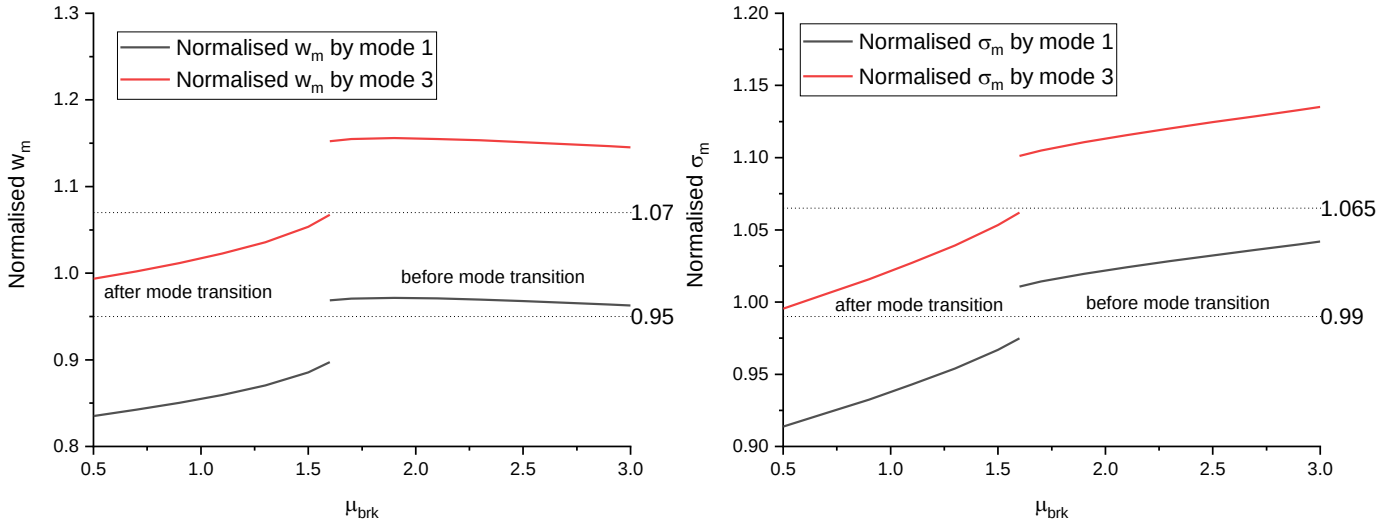

(a) (b)

Fig. 13 Effect of μ_{brk} on the symmetric buckling mode. (a) Normalised w_m. (b) Normalised σ_m. ($\mu_{res} = 0.5$, $w_{init} = 0.3D$, $T_0 = 45$ ℃.)

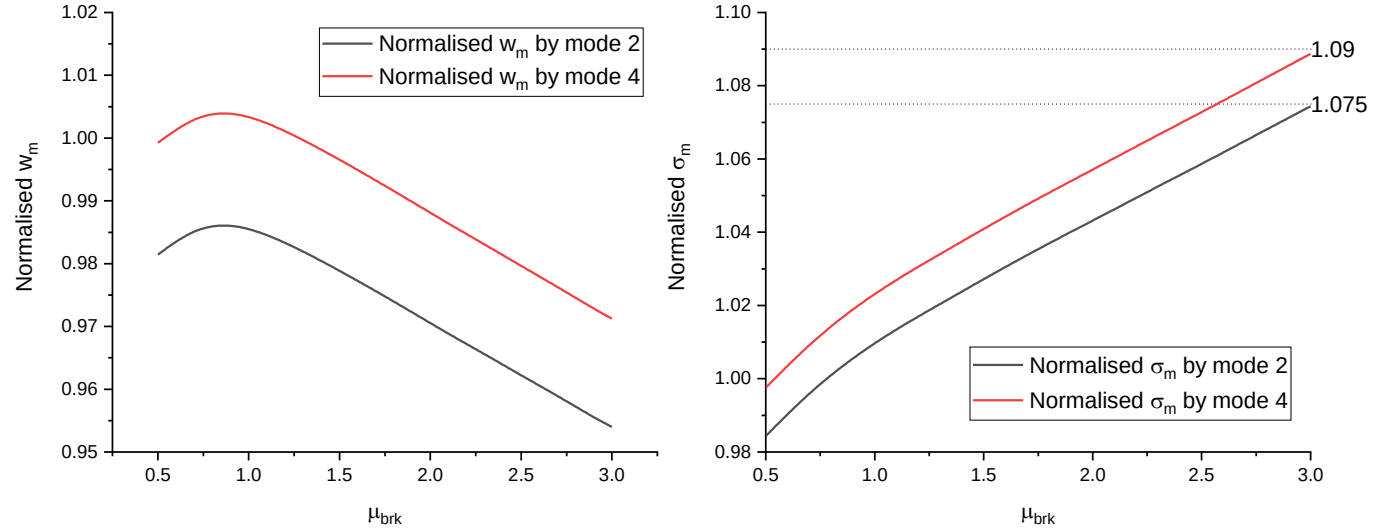

(a) (b)

Fig. 14 Effect of μ_{brk} on the antisymmetric buckling mode. (a) Normalised w_m. (b) Normalised σ_m. ($\mu_{res} = 0.5$, $w_{init} = 0.3D$, $T_0 = 45$ ℃.)

5 Further parameter dependence of mode-jumping temperatures

In Section 4 we saw that the mode-jumping phenomenon essentially disappears for small values of the breakout resistance coefficient μ_{brk}, and also that mode jumping for antisymmetric solutions occurs at much higher temperature differences T_0 than for symmetric solutions. In this section we investigate more widely under what conditions mode jumping disappears, also considering other parameters in the pipe-soil interaction model. To aid our analysis the lower and higher temperature differences at mode jumping are denoted by T_{t1} and T_{t2}, respectively, as indicated in Fig. 6(b).

Fig. 15 illustrates the effect of μ_{brk} on the temperatures T_{t1}, T_{t2}. We see that the mode transition temperature T_{t1} decreases approximately linearly with decreasing μ_{brk} for both symmetric and antisymmetric solutions. The temperature T_{t2} also decreases with decreasing μ_{brk} for both symmetric and antisymmetric solutions but at decreasing rate. As observed before, the values of both T_{t1} and T_{t2} for antisymmetric solutions are much higher than for symmetric solutions. Fig. 15(a) shows that T_{t1} and T_{t2} for symmetric solutions become equal at $\mu_{brk,cs} = 1.32$, while Fig. 15(b) shows that the same happens for antisymmetric solutions at $\mu_{brk,ca} = 1.42$. At these critical values of μ_{brk} the mode jumping phenomenon therefore disappears.

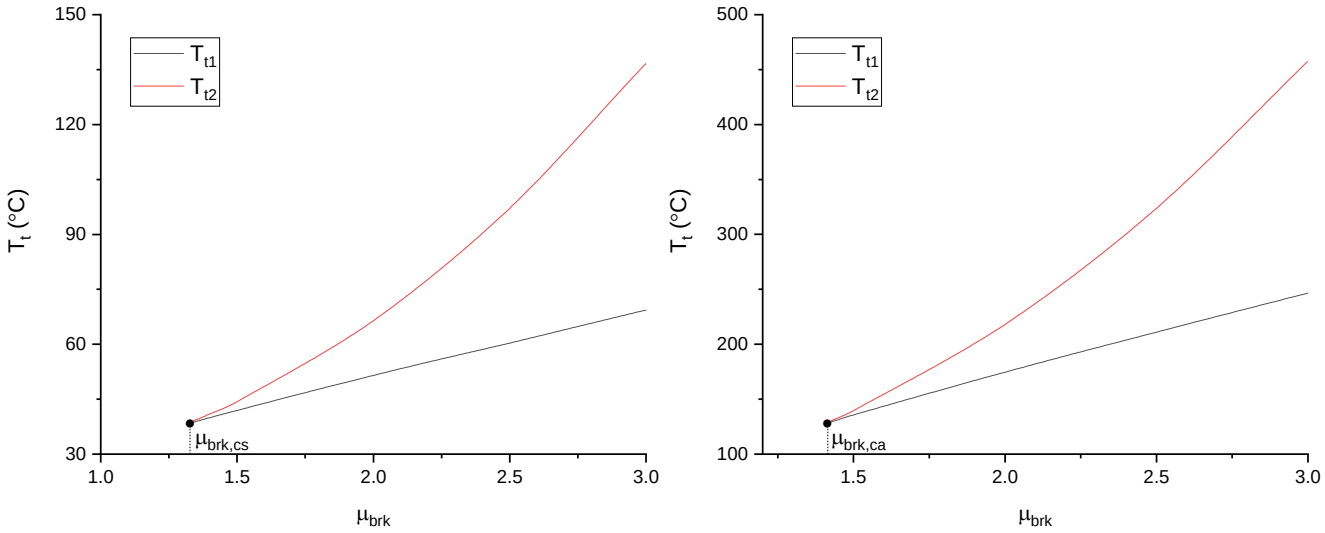

(a) (b)

Fig. 15 Effect of μ_{brk} on the mode jumping temperatures T_{t1} and T_{t2}. (a) Symmetric solutions. (b) Antisymmetric solutions. ($\mu_{res} = 0.5,\ w_{init} = 0.3D$.)

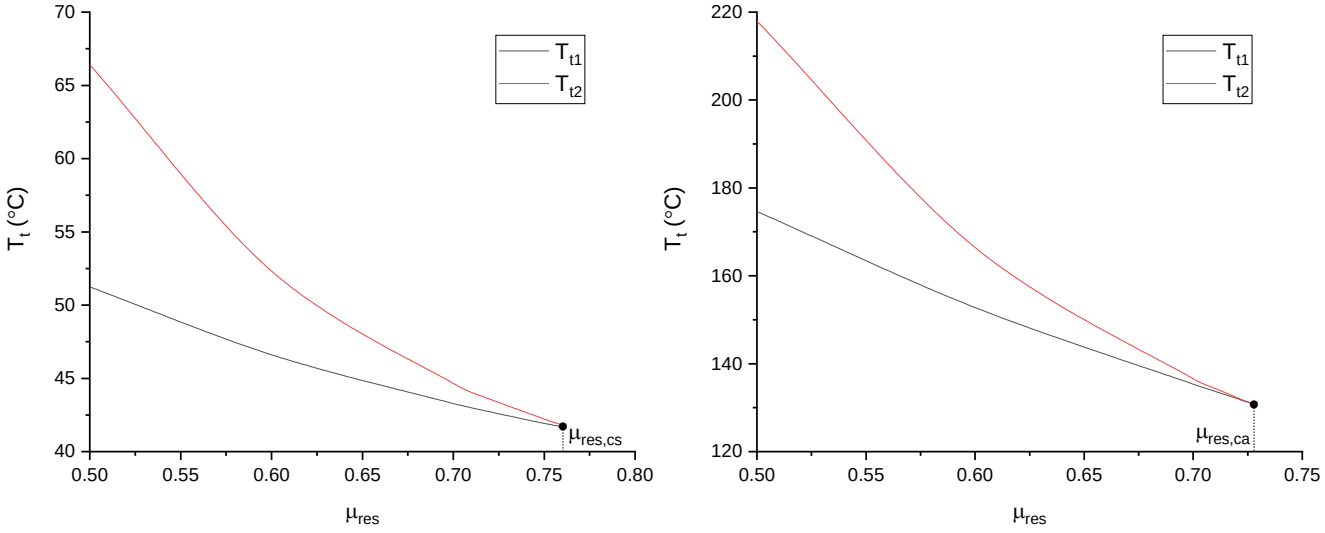

(a) (b)

Fig. 16 Effect of μ_{res} on the mode jumping temperatures T_{t1} and T_{t2}. (a) Symmetric solutions. (b) Antisymmetric solutions. ($\mu_{brk} = 2,\ w_{init} = 0.3D$.)

Fig. 16 illustrates the effect of μ_{res} on the mode jumping temperatures T_{t1} and T_{t2}. Both temperatures decrease with increasing μ_{res}, at decreasing rate. The values of both T_{t1} and T_{t2} for antisymmetric solutions are much larger than those for symmetric solutions, for all μ_{res}. T_{t1} and T_{t2} become equal at $\mu_{res,cs} = 0.762$ for symmetric solutions and at $\mu_{res,ca} = 0.728$ for antisymmetric solutions. At these critical values of μ_{res} the mode jumping phenomenon disappears.

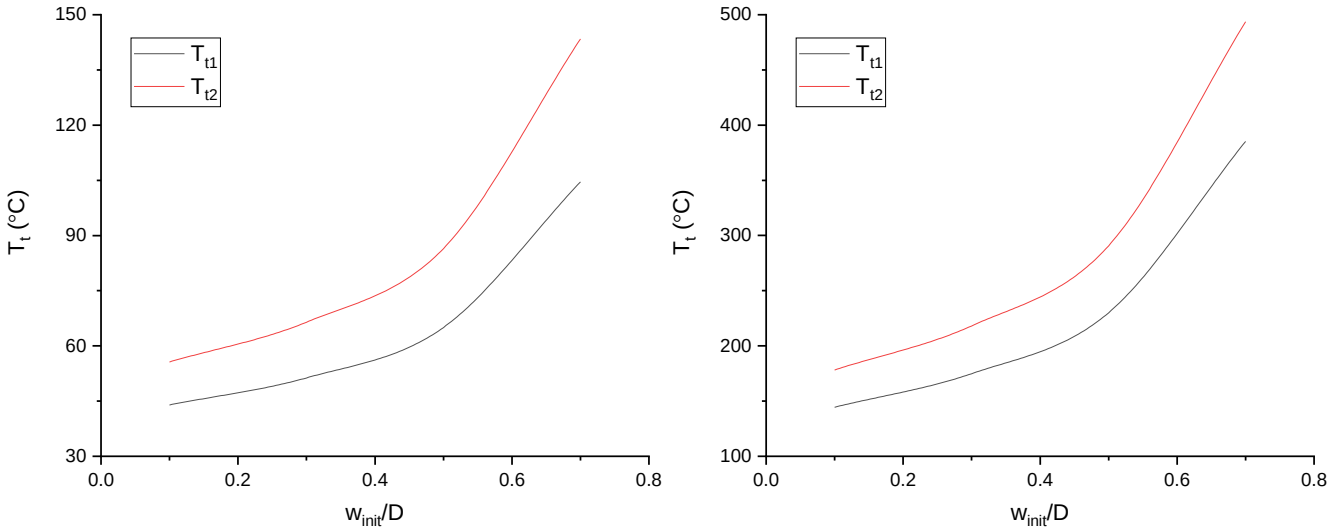

Fig. 17 Effect of w_{init} on the mode transition temperatures T_{t1} and T_{t2}. (a) Symmetric solutions. (b) Antisymmetric solutions. ($\mu_{brk} = 2,\ \mu_{res} = 0.5$.)

Finally, Fig. 17 shows the effect of w_{init} on the temperatures T_{t1} and T_{t2}. Both temperatures increase under increasing w_{init}, at roughly the same rate, for both symmetric and antisymmetric solutions. T_{t1} and T_{t2} never become equal, so we conclude that w_{init} has no effect on the occurrence or not of mode jumping.

6 Conclusions

Lateral buckling of unburied subsea pipelines under high temperature takes the form of localised thermal buckling with the pipeline deflection decaying in an oscillatory pattern with opposite lobes. This buckling pattern is usually investigated analytically by assuming a fixed number of specific lobes in either or both directions, a practice going back to the work of Hobbs [2] who considered four different modes. Real pipeline buckling patterns need not be so easily classified. Also the simple analytical solutions are not available for more realistic nonlinear pipe-soil interaction characteristics. Here we have studied pipeline buckling, subject to a realistic lateral resistance, without making assumptions about the post-buckling pattern. Rather, the pattern is obtained as part of the solution by imposing localised (homoclinic) boundary conditions realistic for long pipelines in which a relatively small segment of pipe is mobilised. This approach has allowed us to predict new jump phenomena that can be identified as transitions between the classical modes. The breakout resistance of the pipe-soil interaction has been found to be a particularly important parameter in whether or not this mode jumping is observed under normal operating conditions of the pipeline.

We make two approximations in our analysis: (1) we assume small deformations, so that a linear Euler-Bernoulli beam model can be used for the pipeline, and (2) the axial compressive force $\bar{P}$ is assumed to be constant in the buckle (to arrive at Eq. (19)). (2) is standard practice in the pipeline literature. In our previous paper [9], in Section 3.4, we justified it by conducting an error analysis in which solutions for minimum and maximum uniform compression in the buckled region are compared. It was found that the error incurred (in both deflections and stresses) is less than 5 %. As to (1), looking at Figs 7 and 8, we have typically $w_m/(2L) = 5/300$ and $w_m/D = 15$. For such deflections one expects beam theory to be entirely adequate.

Although practical standards often aim to avoid buckling, being able to predict post-buckling deflections, forces and stresses is still useful, even if only to ascertain whether buckling would lead to unacceptable stress levels. Indeed, buckling is sometimes artificially induced by means of buckle initiators such as sleepers or buoyancy sections. In such cases the mode-jumping phenomenon studied here may also be observed.

From our parameter studies the following conclusions can be drawn:

(i) Mode jumping may occur between (effectively) modes 1 and 3 for symmetric solutions or between modes 2 and 4 for

antisymmetric solutions when a nonlinear pipe-soil interaction is considered. Under cyclic thermal loading this may lead to undesirable hysteresis cycles with the pipeline snapping back and forth between different modes. For antisymmetric solutions the phenomenon occurs however at much higher temperatures that are outside typical parameter ranges.

(ii) The simple analytical results for Hobbs's modes 1, 2, 3 and 4, obtained with constant lateral resistance, can to some extent be used as useful rough estimates for deflections, forces and stresses in more realistic lateral post-buckling configurations and we have derived some error estimates in Section 4 (Figs 13 and 14). This conclusion makes us confident to use Hobbs's modes 1, 2, 3 and 4 in preliminary design, while in detailed design, our model with nonlinear pipe-soil interaction can be employed to predict the deflections, forces and stresses.

(iii) The mode-jumping phenomenon occurs only when the difference between the breakout resistance and the residual resistance of the pipe-soil interaction is sufficiently large.

Acknowledgments

ZW acknowledges support from the National Natural Science Foundation of China (grant number: 52001229) and the State Key Laboratory of Ocean Engineering (Shanghai Jiao Tong University) (Grant No. GKZD010081).

References

[1] DNVGL-RP-F110. Global buckling of submarine pipelines structural design due to high temperature/high pressure. Oslo: Det Norske Veritas; 2018.

[2] Hobbs RE. In-service buckling of heated pipelines. Journal of Transportation Engineering. 1984;110:175-89.

[3] Taylor N, Gan AB. Refined modelling for the lateral buckling of submarine pipelines. Journal of Constructional Steel Research. 1986;6:143-62.

[4] Liu R, Liu W, Wu X, Yan S. Global lateral buckling analysis of idealized subsea pipelines. Journal of Central South University. 2014;21:416-27.

[5] Karampour H, Albermani F, Gross J. On lateral and upheaval buckling of subsea pipelines. Engineering Structures. 2013;52:317-30.

[6] Hong Z, Liu R, Liu W, Yan S. Study on lateral buckling characteristics of a submarine pipeline with a single arch symmetric initial imperfection. Ocean Eng. 2015;108:21-32.

[7] Shi R, Wang L, Guo Z, Yuan F. Upheaval buckling of a pipeline with prop imperfection on a plastic soft seabed. Thin-Walled Structures. 2013;65:1-6.

[8] Liu R, Wang X. Lateral global buckling high-order mode analysis of a submarine pipeline with imperfection. Applied Ocean Research. 2018;73:107-26.

[9] Wang Z, Tang Y, van der Heijden GHM. Analytical study of distributed buoyancy sections to control lateral thermal buckling of subsea pipelines. Marine Structures. 2018;58:199-222.

[10] Wang Z, Tang Y, van der Heijden GHM. Analytical study of lateral thermal buckling for subsea pipelines with sleeper. Thin-Walled Structures. 2018;122:17-29.

[11] Zhu J, Attard MM, Kellermann DC. In-plane nonlinear localised lateral buckling of straight pipelines. Engineering Structures. 2015;103:37-52.

[12] Zeng X, Duan M. Mode localization in lateral buckling of partially embedded submarine pipelines. International Journal of Solids and Structures. 2014;51:1991-9.

[13] Wang Z, van der Heijden GHM. Localised lateral buckling of partially embedded subsea pipelines with nonlinear soil resistance. Thin-Walled Structures. 2017;120:408-20.

[14] Chatterjee S, White DJ, Randolph MF. Numerical simulations of pipe-soil interaction during large lateral movements on clay. Géotechnique. 2012;62:693-705.

[15] White DJ, Cheuk CY. Modelling the soil resistance on seabed pipelines during large cycles of lateral movement. Marine Structures. 2008;21:59-79.

[16] Hunt GW, Bolt H, Thompson J. Structural localization phenomena and the dynamical phase-space analogy. Proceedings of the Royal Society A. 1989;425:245-67.

[17] van der Heijden GHM, Champneys AR, Thompson JMT. The spatial complexity of localized buckling in rods with noncircular cross section. SIAM Journal on Applied Mathematics. 1998;59:198-221.

[18] Champneys AR, Spence A. Hunting for homoclinic orbits in reversible systems: a shooting technique. Advances in Computational Mathematics. 1993;1:81-108.